Chapter One

Introduction

1.1 Bone and the Skeletal System

Bone is a phenomenal tissue and the main component of our skeletal system. Apart from giving us shape and form, bone performs several important functions. These include support, protection, movement, mineral storage and, indirectly, blood cell formation (32).

Bones are organs. Even though the major component of bone is osseous (bone) tissue, bones are intimately associated with cartilage, fibrous connective tissue, nervous tissue, muscle and epithelial tissue. In general, the anatomy of bone can be considered at three levels: macroscopic, microscopic and chemical (11, 32).

1.2 Macroscopic Structure

Most long bones have the same general structure (Figure 1.1), consisting of the shaft, or diaphysis, which is composed of relatively thick cortical bone that surrounds the medullary cavity. The epiphyses, or the ends, are generally more expanded than the diaphysis and are composed of cortical bone on the exterior and trabecular bone on their interior. The joint surfaces of the epiphyses are covered with a layer of articular cartilage that acts as a cushion and lubricating surface between joints (32).

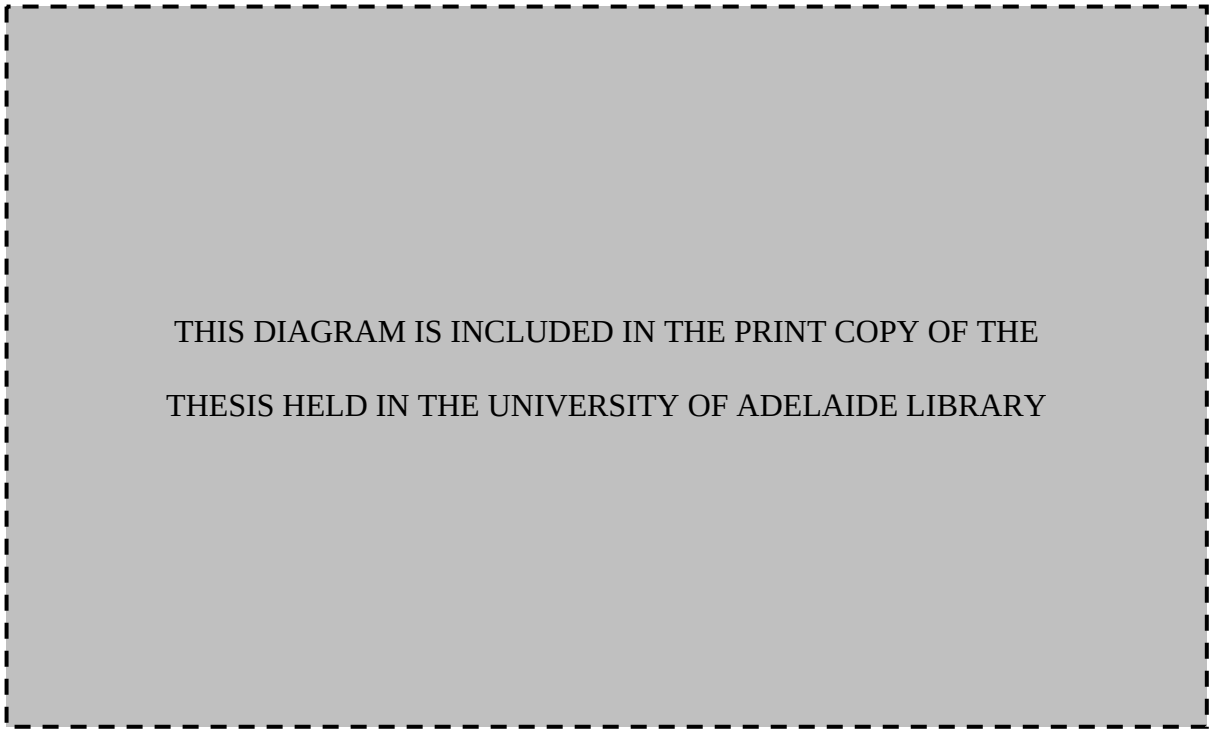

Figure 1.1 Illustration of a long bone showing the diaphysis, epiphyses, medullary cavity, cortical and trabecular bone (32). Reprinted by permission of Pearson Education Inc.

Special membranes line both the external and internal bone surfaces. The outer surface is covered and protected by a double-layered membrane called the periosteum. The periosteum is composed of an outer fibrous layer and an inner osteogenic layer. This later layer consists primarily of osteoblasts (bone forming cells) and osteoclasts (bone resorbing cells). The internal bone surfaces are covered with a membrane, called the endosteum. This membrane lines the trabeculae of the trabecular bone and lines canals that pass through the cortical bone.

The other bones of the body (Figure 1.2) essentially all consist of thin periosteum covered plates of cortical bone on the outside and endosteum lined trabecular bone on the inside.

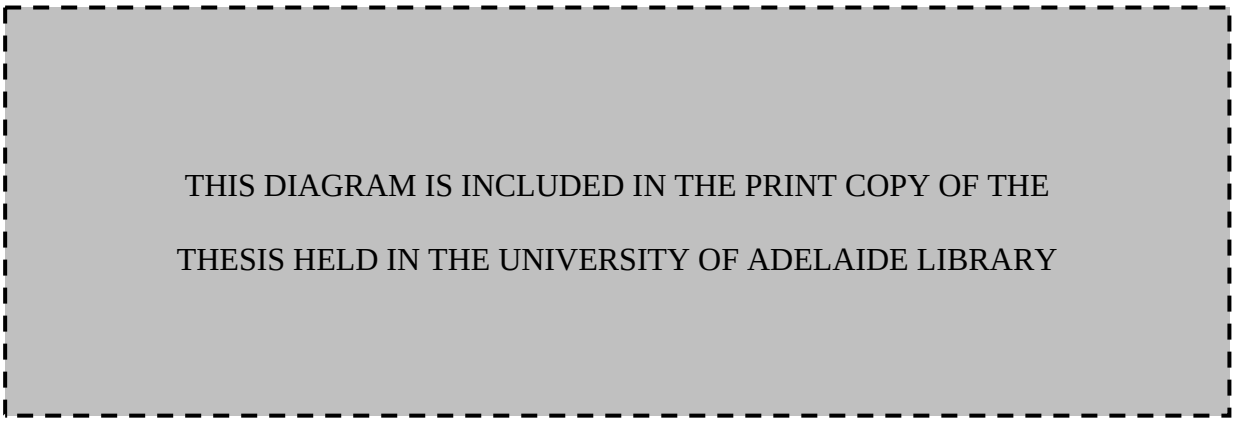

Figure 1.2 Illustration of the different bone types with the body (32). Reprinted by permission of Pearson Education Inc.

1.3 Microscopic Structure

Cortical bone appears very dense to the unaided eye. However, closer inspection reveals a porous structure, comprising of canals and passageways that act as openings for nerves, blood vessels and lymphatic vessels. The structural unit of cortical bone is termed the osteon or Haversian system. Each of these units consists of an elongated cylinder oriented parallel to the long axis of the bone. In a functional sense these structural units can be thought of as tiny weight-bearing pillars (11, 32).

Each osteon is a group of concentric cylinders of bone matrix. Each of these hollow cylinders is called a lamellae. Collagen fibers in a particular lamella run in a single direction, while collagen fibers in adjacent lamellae always run in the opposite direction. This arrangement is designed so as to withstand torsional (twisting) stresses.

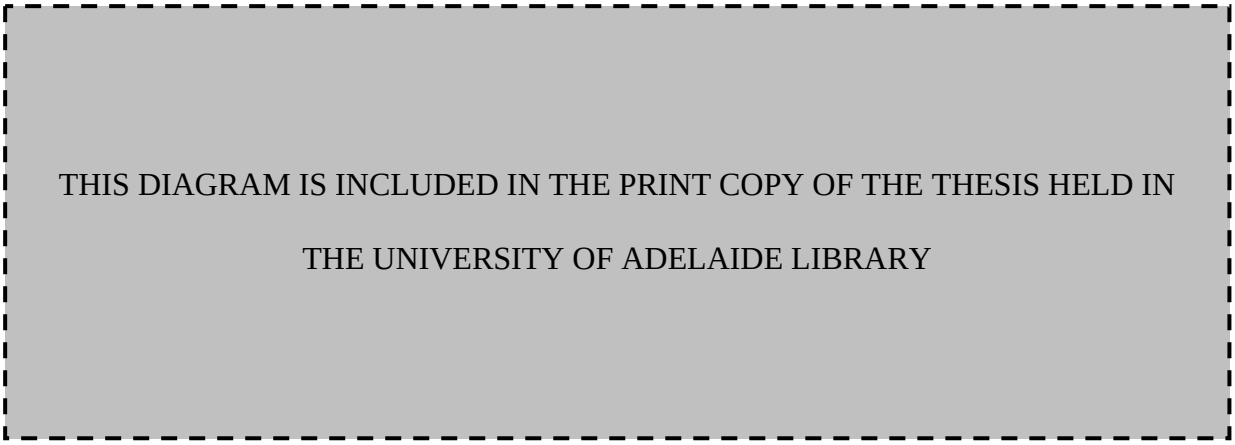

Figure 1.3 Illustration of the osteon showing the arrangement of adjacent collagen fibers (32). Reprinted by permission of Pearson Education Inc.

In contrast to cortical bone, trabecular bone is comprised of trabeculae, which form a spongy porous network (Figure 1.4). This combination of structures maximises whole bone strength while minimising weight (58).

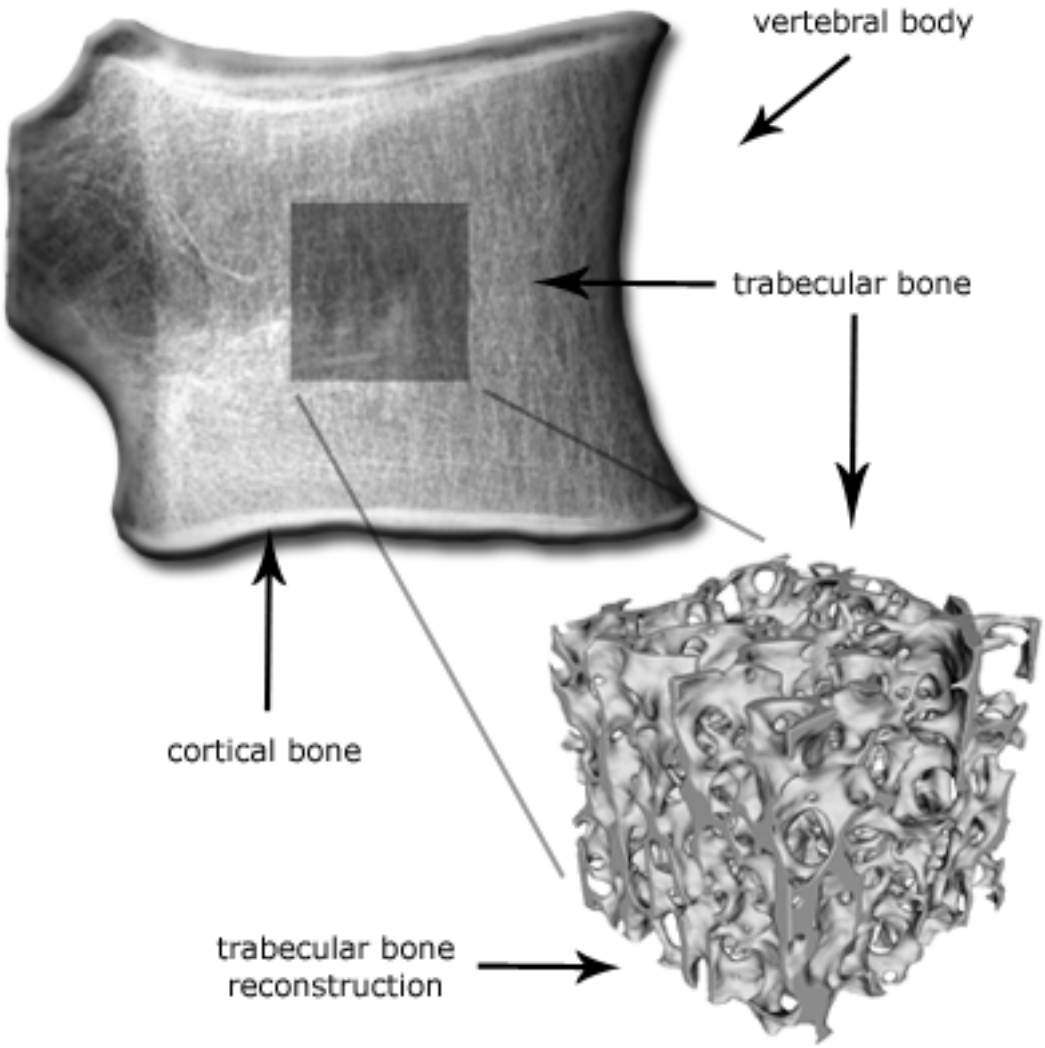

Figure 1.4 Examples of cortical and trabecular bone from a vertebral body. Image illustrates a lateral X-ray of a vertebral body (top left) and a reconstruction of the trabecular bone taken from the centrum of the vertebral body (bottom right).

1.4 Chemical Composition

Bone consists of both organic and inorganic phases. The organic matrix, which accounts for approximately 35% of the total dry weight of bone, includes bone-specific proteins, osteoclasts, osteoblasts and osteoid (58). The osteoid includes organic components such as proteoglycans, glycoproteins and collagen elements, all of which are made and deposited by osteoblasts. The flexibility and great tensile strength of bone is in part a contribution of these organic elements, in particular collagen (11, 32).

The inorganic components, which account for approximately 65% of the total dry weight of bone, consist primarily of mineral salts, or hydroxyapatites that are predominantly calcium phosphate, $Ca_{10}(PO_4)_6(OH)_{2,}$ based (58). Tiny calcium salt crystals lie within and around the collagen fibers and account for the most notable characteristic of bone; it's compression resistance. It is the proper combination of organic and inorganic elements that allows bone to be extremely durable and strong without being brittle. Interestingly, bone has been shown to be half as strong as steel in resisting compression and fully as strong as steel in resisting tension (32).

1.5 Bone Homeostasis

Even though bone appears to be lifeless, and in most people conjures images of graveyards, bone is a very dynamic and active tissue. Large amounts of bone are continually being removed and replaced. Every year 5-10% of the existing bone mass is replaced through a process termed bone remodelling (32, 58). Through the process of bone resorption and formation, bone remodelling maintains the mechanical integrity of the skeleton by replacing old bone with new bone (58). This process is closely coupled and coordinated by groups of osteoblasts and osteoclasts. In a young healthy adult skeleton the total bone mass remains constant, indicating that the rates of resorption and deposition are equal.

1.5.1 Control of Remodelling

In order for such dynamic remodelling to occur, tight regulation must be in place. Skeletal remodelling is thought to be controlled by two different control loops. A hormonal mechanism operates via negative feedback to maintain plasma calcium levels, while the other mechanism involves responses to mechanical and gravitational stimuli. Even though an important factor, the hormonal control mechanisms are beyond the scope of this study and will not be discussed.

Mechanical control loops are more directly associated with the physical architecture of the bone. This type of control essentially keeps bones strong where stressors are the greatest. The general consensus is that bone will remodel in response to forces that are placed upon it (11, 12, 58). Observations in support of this idea include:

- Long bones exhibit the greatest thickness mid way along their shaft, where bending stresses would be the greatest.
- Curved bones exhibit greatest thickness in regions where they are most likely to buckle.
- Trabecular bone aligns along lines of force (Figure 1.5), and large, bony projections are always present at the sites where heavy, active muscles attach.

THIS DIAGRAM IS INCLUDED IN THE PRINT COPY OF THE THESIS HELD IN THE UNIVERSITY OF ADELAIDE LIBRARY

Figure 1.5 Images illustrating the alignment of trabecular bone in accordance with the lines of force (32). [a] Actual X-ray of a proximal femur and [b] diagram illustrating the stressors on the proximal femur. Reprinted by permission of Pearson Education Inc.

In all, the skeleton is continuously under both hormonal and mechanical influences. It is speculated that the hormonal loop is responsible for determining global skeletal remodelling (in response to plasma calcium levels), while the mechanical loop and microdamage determine local remodelling, as bones in least stressed areas are more dispensable (11, 12, 32).

1.6 Bone Quality

In the simplest sense, bone quality may be defined as a measure of how well the bone is capable of performing its functional role. Bone quality is dependent on a number of factors, including the amount of bone, the microarchitecture, mineralisation of bone, organic constituents, activity of cells and the low level molecular signalling. However, for the purpose of this thesis, bone quality will be thought of as depending on only the apparent parameters:

- Bone volume fraction (BV/TV): The amount of bone occupying a given volume.
- Bone microarchitecture: The specific alignment, shape and size of trabeculae in a given volume.

Studies have shown BV/TV to be a strong predictor of mechanical properties, accounting for 89-94% of the variability of ultimate stresses (43) and accounting for 92% of the variability in maximum compressive strength (33). Architectural parameters such as trabeculae thickness and separation, connectivity and spatial geometry have key roles in determining bone quality. Studies have shown bone microarchitecture related factors may explain 10 – 30% of the variability in bone mechanical competence, beyond that of bone mass (10). However, it should be kept in mind that factors such as age and pathologies also have an influence on the mechanical competence of bone.

The effects of aging on ultimate stress have been reported in a number of studies. Mosekilde *et al* (34-36, 38) showed that ultimate stress is reduced by an average of almost 7% per decade for the

human proximal femur and by almost 11% per decade for vertebral bodies from ages 20 to 100 years, due mostly to decreases in BV/TV. In addition, because trabecular bone is anisotropic (Section 1.9 and Chapter 3), its strength also depends on orientation of the specimen with respect to loads. This dependence has also been reported as changing with age (9, 34, 35).

When all these findings are considered together, it is clear that the mechanical properties of trabecular bone vary substantially with anatomical site and age, reflecting underlying variations in volume fraction and microarchitecture. Trabecular strength can therefore be considered as heterogeneous, anisotropic and asymmetric (different between tension and compression) (3, 9, 11-13, 30, 35, 37, 39, 40, 54).

1.7 Osteoporosis

Osteoporosis refers to a systemic disease where an imbalance of bone remodelling occurs. The composition of the bone matrix, bone mass and architecture are compromised, making the bone more porous and lighter (25, 32, 57).

The World Health Organization (WHO) defines osteoporosis as a disease that is characterized by a reduction of bone mass and a deterioration of the architecture of the bone leading to increased bone fragility (1, 57). The lifetime risk for hip, vertebral and wrist fractures, resulting from osteoporosis, has been estimated at 40%, similar to coronary heart disease, and is three time more likely in women than in men (57). The WHO has developed criteria for diagnosis of osteoporosis, which are used daily worldwide. These criteria are based on comparing bone mineral density (BMD) (Section 1.8) in a particular patient with those of a referent “normal” population. Values, which fall well below the average for the normal (stated statistically as 2.5 standard deviations below the average), are diagnosed as osteoporotic, values less than the normal, but not 2.5 standard deviations below the average are classified as osteopenic (meaning a decreased bone mineral density) (56).

1.8 Assessment of Trabecular Bone

1.8.1 Dual Energy X-ray Absorptiometry

Dual energy X-ray absorptiometry (DXA) is considered the gold standard in bone assessment (56). The dual-energy component refers to the dual energy x-ray spectra, obtained either by filtering or dual excitation. In single energy absorptiometry techniques, differences in attenuation due to varying soft tissue thickness can not be distinguished from bone density differences. As such, single energy absorptiometry techniques commonly require soft tissue equivalent material to be present in order to eliminate soft tissue artifacts. DXA overcomes this problem by mathematically subtracting the soft tissue attenuation from the measured attenuation (15, 28)

DXA is a projection based technique that estimates the amount of bone present in a region using X-ray attenuation information. However, measured BMD is an areal density (expressed as g/cm^2) and not a true volumetric density (expressed as g/cm^3). This makes DXA and BMD measures prone to bone size artifacts. As such, BMD measures from men are observed to be higher than those of women, based purely on skeletal size differences (14, 15). This same problem creates complications in BMD measurements of young children. Even though the measurement of BMD is a useful clinical tool in predicting fracture risk (56), there are significant degrees of discrepancies in BMD measurements of patients who have been diagnosed as high risk and high risk patients who actually fracture (26, 27). BMD explains between 30 – 80 % of the variability in bone mechanical competence (10) and it is this large variability that requires consideration and the development of other techniques and measures. However, despite these shortcomings, DXA is the current gold standard in the assessment of fracture risk prediction and is the clinical assessment tool recognized by the WHO.

1.8.2 Quantitative Ultrasound

Clinical quantitative ultrasound (QUS) utilizes the transmission of high frequency sound and the resulting attenuation of that sound through bone, in order to assess bone material properties (15, 26,

28, 56). Unlike the electromagnetic wave interrogation of X-ray based techniques, QUS utilizes mechanical vibration. This mechanical interaction of high frequency sound with bone results in two primary measures. The speed of sound (SOS) and the broadband ultrasound attenuation (BUA) (15, 28). Even though utilizing a completely different mechanism of interaction with the bone, QUS measurements correlate reasonably well with x-ray based DXA BMD measurements (28). Evidence has also been shown to support their use for assessment of fracture risk (24).

1.8.3 Computed Tomography

Quantitative computed tomography (CT) is the only current *in-vivo* technology capable of true volumetric density measurement (15, 26). Clinically, quantitative CT is used to measure bone density (g/cm^3) in the spine. The standard involves scanning a single 8 – 10 mm slice through 3 – 4 vertebral bodies. The scan is always accompanied by a scan of a calibration standard. From the reconstructed CT images, the average attenuation of the vertebral body bone is calculated along with the attenuation of the calibration standard. Then via a transformation of the known attenuation to density of the standard, the volumetric density of the vertebral body and its sub-compartments can be estimated (15, 26, 28, 56). Although quantitative CT does provide information on the shape and architecture of bone, the current resolution of standard CT systems are not capable of resolving the trabecular bone (15, 28, 56). Other disadvantages include relatively high radiation exposure and costs (56).

Micro-computed tomography (µCT) systems operate in a similar manner to standard CT, but are capable of resolutions down to 1 µm (28). The trade-off for achieving such resolutions is that the specimen must be small in size. *In-vivo* imaging at these resolutions is not yet available for human trabecular bone. However, the µCT modality can be utilized as a tool for extracting relevant information from human bone samples at resolutions suitable for trabecular bone assessment (49, 50). This modality can be used as a gold standard in the non-invasive assessment of trabecular bone *ex-vivo*.

1.8.4 Radiography

Often, late stage osteoporosis can be diagnosed from a plain X-ray (56), which, is the most commonly assessable and cheapest imaging modality in the world. Radiographically detected change in apparent bone density, abnormalities in trabecular architecture, cortical width and visible evidence of fracture are all accessible through macroscopic visual inspection of plain X-rays (56). More detailed quantitative assessment of trabecular architecture has also been attempted.

One of the first radiographic techniques was developed by Singh *et al* (52). In this technique, subjective ratings of the appearance of the trabecular pattern were made on X-rays of the proximal femur. Rockoff *et al* (44-48) also pioneered work utilizing the information contained in radiographic images for assessing trabecular bone architecture. In more recent years a number of quantitative techniques have been developed, which are based on textural and fractal analyses of the radiographic trabecular pattern. Geraets *et al* (17-22) developed techniques to measure information about the trabecular pattern from binarised radiographs. Luo *et al* (31) were able to demonstrate a clear relationship between the 3D structure and 2D projection of trabecular bone. Caldwell *et al* (5) showed that the addition of structural information, measured from plain radiographs, to that of bone mass was more superior in explaining the variability in mechanical strength than mass alone. Chappard *et al* were able to show textural indices obtained from radiographs correlated with histomorphometric parameters (8) and also demonstrated that a radiographic measure of anisotropy was able to distinguish individuals with vertebral fractures from controls (7). The use of fractal dimension, Moire pattern and textural anisotropy to characterize trabecular bone microarchitecture have also been investigated by others (2, 4, 6, 28, 51).

1.9 Anisotropic Properties of Trabecular Bone

The structural property of an object is anisotropic if the property differs in character or quantity according to direction. Anisotropy in trabecular bone is evident in both strength (16, 29, 30, 35, 38) and modulus (9, 29, 30, 35, 38). This anisotropic mechanical behaviour is thought to develop as a form of adaptive response to functional loading and is known to increase as trabecular bone becomes more porous (30).

A number of studies have considered monotonic failure mechanics of trabecular bone in orthogonal directions (16, 38, 40). These studies all report anisotropic mechanical differences of the order of 2 to 3 times between superoinferior and transverse directions. Mosekilde *et al* (1985) also showed that the anisotropic strength ratio (ratio of longitudinal to transverse strength) increases with age (40), highlighting that trabecular bone mechanical anisotropy is an important characteristic of trabecular bone. The principal directions of trabecular bone, which give rise to this anisotropic property, have been shown to be aligned with the principal structural directions of the trabecular bone (41). This observation indicates that the mechanical anisotropy and structural anisotropy are linked. Thus, measurements of mechanical anisotropy can be made through measurements of structural anisotropy (41).

Since trabecular bone's mechanical properties are anisotropic, scalar measures of the amount of bone, such as BV/TV, can not completely explain all its mechanical characteristics (55). Trabecular bone mechanical properties must, therefore, be dependent not only on the amount of bone but some directionally dependent architectural property, such as structural anisotropy. This phenomenon has been reported in the literature. Ulrich *et al* (1998) were able to explain 53% of the variability of mechanical properties of trabecular bone samples using BV/TV alone. This was increased to 82% by adding a measure of structural anisotropy (53). Similarly, Goulet *et al* (1994) were able to account for up to 90% of the variability in mechanical properties by using a combination of BV/TV and structural anisotropy parameters (23).

1.10 Objectives and Overview of the Thesis

Trabecular microarchitecture and structural anisotropy of trabecular bone are important characteristics that may have significant clinical implications in bone quality assessment. The ability to assess these characteristics non-invasively would be of great importance to public health worldwide. However, in addition to the assessment of structural characteristics, further insight into the mechanics of trabecular bone is also needed.

Therefore, the focus of this thesis was to gain insight into some of the mechanical properties of trabecular bone and implement strategies for the assessment of trabecular architecture and trabecular structural anisotropy from non-invasive X-ray (projection) based information. Specifically, the following questions were posed:

- Can the structural anisotropy of trabecular bone be extracted from the projection of the trabecular architecture?
- Can projection based structural anisotropy improve the understanding of trabecular bone mechanical properties?
- Does the structural basis of trabecular bone mechanical properties change with overload in the orthogonal direction and can projection based structural anisotropy characterize this change?

To investigate trabecular bone's anisotropic properties, mechanical testing was carried out on trabecular bone samples in two orthogonal directions (Chapter 4). To investigate if the structural basis of trabecular bone mechanical properties changes with overload, a second overload, orthogonal to the initial overload, was also carried out (Chapter 4). For the assessment of trabecular structural anisotorpy, two novel measures were proposed and their properties investigated (Chapters 5 and 6). The ability of these measures to explain the variance in mechanical properties after initial and second overloads was explored (Chapter 7).

References

1. Consensus development conference: prophylaxis and treatment of osteoporosis. Osteoporos Int 1:114-7; 1991.
2. Benhamou, C. L., Lespessailles, E., Jacquet, G., Harba, R., Jennane, R., Loussot, T., Tourliere, D., and Ohley, W. Fractal organization of trabecular bone images on calcaneus radiographs. J Bone Miner Res 9:1909-18; 1994.
3. Brinckmann, P., Biggemann, M., and Hilweg, D. Prediction of the compressive strength of human lumbar vertebrae. Spine 14:606-10; 1989.
4. Buckland-Wright, J. C., Lynch, J. A., Rymer, J., and Fogelman, I. Fractal signature analysis of macroradiographs measures trabecular organization in lumbar vertebrae of postmenopausal women. Calcif Tissue Int 54:106-12; 1994.
5. Caldwell, C. B., Willett, K., Cuncins, A. V., and Hearn, T. C. Characterization of vertebral strength using digital radiographic analysis of bone structure. Med Phys 22:611-5; 1995.
6. Caligiuri, P., Giger, M. L., Favus, M. J., Jia, H., Doi, K., and Dixon, L. B. Computerized radiographic analysis of osteoporosis: preliminary evaluation. Radiology 186:471-4; 1993.
7. Chappard, C., Brunet-Imbault, B., Lemineur, G., Giraudeau, B., Basillais, A., Harba, R., and Benhamou, C. L. Anisotropy changes in post-menopausal osteoporosis: characterization by a new index applied to trabecular bone radiographic images. Osteoporos Int; 2005.
8. Chappard, D., Guggenbuhl, P., Legrand, E., Basle, M. F., and Audran, M. Texture analysis of X-ray radiographs is correlated with bone histomorphometry. J Bone Miner Metab 23:24-9; 2005.
9. Ciarelli, M. J., Goldstein, S. A., Kuhn, J. L., Cody, D. D., and Brown, M. B. Evaluation of orthogonal mechanical properties and density of human trabecular bone from the major metaphyseal regions with materials testing and computed tomography. J Orthop Res 9:674-82; 1991.
10. Cortet, B., and Marchandise, X. Bone microarchitecture and mechanical resistance. Joint Bone Spine 68:297 - 305; 2001.
11. Currey, J. D. Bones - Structure and Mechanics. Princeton University Press; 2002.
12. Currey, J. D. The many adaptations of bone. J Biomech 36:1487-95; 2003.
13. Dempster, D. W. Bone microarchitecture and strength. Osteoporos Int 14 Suppl 5:54-6; 2003.
14. Faulkner, K. G., Gluer, C. C., Majumdar, S., Lang, P., Engelke, K., and Genant, H. K. Noninvasive measurements of bone mass, structure, and strength: current methods and experimental techniques. AJR Am J Roentgenol 157:1229-37; 1991.
15. Faulkner, K. G., and Pocock, N. Future methods in the assessment of bone mass and structure. Best Pract Res Clin Rheumatol 15:359-83; 2001.
16. Galante, J., Rostoker, W., and Ray, R. D. Physical properties of trabecular bone. Calcif Tissue Res 5:236-46; 1970.
17. Geraets, W., and Van der Stelt, P. Analysis of the radiographic trabecular pattern. Pattern Recognition Letters 12:575-581; 1991.
18. Geraets, W. G. Comparison of two methods for measuring orientation. Bone 23:383-8; 1998.
19. Geraets, W. G., Van der Stelt, P. F., and Elders, P. J. The radiographic trabecular bone pattern during menopause. Bone 14:859-64; 1993.
20. Geraets, W. G., Van der Stelt, P. F., Lips, P., Elders, P. J., Van Ginkel, F. C., and Burger, E. H. Orientation of the trabecular pattern of the distal radius around the menopause. J Biomech 30:363-70; 1997.
21. Geraets, W. G., Van der Stelt, P. F., Lips, P., and Van Ginkel, F. C. The radiographic trabecular pattern of hips in patients with hip fractures and in elderly control subjects. Bone 22:165-73; 1998.
22. Geraets, W. G., Van der Stelt, P. F., Netelenbos, C. J., and Elders, P. J. A new method for automatic recognition of the radiographic trabecular pattern. J Bone Miner Res 5:227-33; 1990.
23. Goulet, R. W., Goldstein, S. A., Ciarelli, M. J., Kuhn, J. L., Brown, M. B., and Feldkamp, L. A. The relationship between the structural and orthogonal compressive properties of trabecular bone. J Biomech 27:375-89; 1994.
24. Gregg, E. W., Kriska, A. M., Salamone, L. M., Roberts, M. M., Anderson, S. J., Ferrell, R. E., Kuller, L. H., and Cauley, J. A. The epidemiology of quantitative ultrasound: a review of the relationships with bone mass, osteoporosis and fracture risk. Osteoporos Int 7:89-99; 1997.
25. Jee, W. S. S. Integrated Bone Tissue Physiology: Anatomy and Physiology. In: S. C. Cowin (ed.), Bone Mechanics Handbook, pp. 1/1 - 1/68. New York: CRC Press; 2001.
26. Kanis, J. A. Diagnosis of osteoporosis and assessment of fracture risk. Lancet 359:1929-36; 2002.
27. Kanis, J. A., Johnell, O., Oden, A., Dawson, A., De Laet, C., and Jonsson, B. Ten year probabilities of osteoporotic fractures according to BMD and diagnostic thresholds. Osteoporos Int 12:989-95; 2001.
28. Kaufman, J. J. S., R. S. Noninvasive Measurement of Bone Integrity. In: S. C. Cowin (ed.), Bone Mechanics Handbook, pp. 34/1 - 34/35: CRC Press; 2001.
29. Keaveny, T. M., and Hayes, W. C. A 20-year perspective on the mechanical properties of trabecular bone. J Biomech Eng 115:534-42; 1993.
30. Keaveny, T. M., Morgan, E. F., Niebur, G. L., and Yeh, O. C. Biomechanics of trabecular bone. Annu Rev Biomed Eng 3:307-33; 2001.
31. Luo, G., Kinney, J. H., Kaufman, J. J., Haupt, D., Chiabrera, A., and Siffert, R. S. Relationship between plain radiographic patterns and three- dimensional trabecular architecture in the human calcaneus. Osteoporos Int 9:339-45; 1999.
32. Marieb, E. N. Human Anatomy and Physiology: Benjamin Cummings; 1998.
33. McCalden, R. W., McGeough, J. A., and Court-Brown, C. M. Age-related changes in the compressive strength of cancellous bone. The relative importance of changes in density and trabecular architecture. J Bone Joint Surg Am 79:421-7; 1997.
34. Mosekilde, L. Age-related changes in vertebral trabecular bone architecture--assessed by a new method. Bone 9:247-50; 1988.
35. Mosekilde, L. Normal vertebral body size and compressive strength: relations to age and to vertebral and iliac trabecular bone compressive strength. Bone 7:207-12; 1986.
36. Mosekilde, L. Sex differences in age-related loss of vertebral trabecular bone mass and structure--biomechanical consequences. Bone 10:425-32; 1989.
37. Mosekilde, L. Vertebral structure and strength in vivo and in vitro. Calcif Tissue Int 53 Suppl 1:S121-5; discussion S125-6; 1993.
38. Mosekilde, L., and Danielsen, C. C. Biomechanical competence of vertebral trabecular bone in relation to ash density and age in normal individuals. Bone 8:79-85; 1987.
39. Mosekilde, L., Ebbesen, E. N., Tornvig, L., and Thomsen, J. S. Trabecular bone structure and strength - remodelling and repair. J Musculoskelet Neuronal Interact 1:25-30; 2000.
40. Mosekilde, L., and Viidik, A. Correlation between the compressive strength of iliac and vertebral trabecular bone in normal individuals. Bone 6:291-5; 1985.
41. Odgaard, A., Kabel, J., van Rietbergen, B., Dalstra, M., and Huiskes, R. Fabric and elastic principal directions of cancellous bone are closely related. J Biomech 30:487-95; 1997.
42. Oh, W., and Lindquist, W. B. Image Thresholding by Indicator Kriging. IEEE Transaction on Pattern Analysis and Machine Intelligence 21:590-602; 1999.

43. Pothuaud, L., Van Rietbergen, B., Mosekilde, L., Beuf, O., Levitz, P., Benhamou, C. L., and Majumdar, S. Combination of topological parameters and bone volume fraction better predicts the mechanical properties of trabecular bone. J Biomech 35:1091-9; 2002.
44. Rockoff, S. D. Quantitative microdensitometric x-ray analysis of vertebral trabecular bone. A preliminary report. Radiology 88:794-6; 1967.
45. Rockoff, S. D. Radiographic trabecular quantitation of human lumbar vertebrae in situ. I. Theory and method for study of osteoporosis. Invest Radiol 2:272-89; 1967.
46. Rockoff, S. D. Techniques of data extraction from radiological images. An overview. Invest Radiol 7:206-22; 1972.
47. Rockoff, S. D., Scandrett, J., and Zacher, R. Quantitation of relevant image information: automated radiographic bone trabecular characterization. Radiology 101:435-9; 1971.
48. Rockoff, S. D., Zettner, A., and Albright, J. Radiographic trabecular quantitation of human lumbar vertebrae in situ. II. Relation to bone quantity, strength and mineral content (preliminary results). Invest Radiol 2:339-52; 1967.
49. Ruegsegger, P. Imaging of Bone Structure. In: S. C. Cowin (ed.), Bone Mechanics Handbook, pp. 9/1 - 9/24: CRC Press; 2001.
50. Ruegsegger, P., Koller, B., and Muller, R. A microtomographic system for the nondestructive evaluation of bone architecture. Calcif Tissue Int 58:24-9; 1996.
51. Siffert, R. S. L., G. Kaufman, J. J. Moire patterns from plain radiographs of trabecular bone. Proceedings of the 17th Annual Conference of the IEEE Engineering in Medicine and Biology Society 1:545 - 546; 1995.
52. Singh, M., Nagrath, A. R., and Maini, P. S. Changes in trabecular pattern of the upper end of the femur as an index of osteoporosis. J Bone Joint Surg Am 52:457-67; 1970.
53. Ulrich, D., van Rietbergen, B., Laib, A., and Ruegsegger, P. The ability of three-dimensional structural indices to reflect mechanical aspects of trabecular bone. Bone 25:55-60; 1999.
54. Vesterby, A., Mosekilde, L., Gundersen, H. J., Melsen, F., Holme, K., and Sorensen, S. Biologically meaningful determinants of the in vitro strength of lumbar vertebrae. Bone 12:219-24; 1991.
55. Waarsing, J. H., Day, J. S., and Weinans, H. Longitudinal micro-CT scans to evaluate bone architecture. J Musculoskelet Neuronal Interact 5:310-2; 2005.
56. WHO Technical Report Series (Prevention and Management of Osteoporosis) - Diagnosis and Assessment. In: W. S. G. o. P. a. M. o. Osteoporosis (ed.), WHO Scientific Group on Prevention and Management of Osteoporosis, pp. 53(33): World Health Organization; 2003.
57. WHO Technical Report Series (Prevention and Management of Osteoporosis) - Introduction. In: W. S. G. o. P. a. M. o. Osteoporosis (ed.), WHO Scientific Group on Prevention and Management of Osteoporosis, pp. 1(9): World Health Organization; 2003.
58. WHO Technical Report Series (Prevention and Management of Osteoporosis) - Pathogenesis of Osteoporosis and Related Fractures. In: W. S. G. o. P. a. M. o. Osteoporosis (ed.), WHO Scientific Group on Prevention and Management of Osteoporosis, pp. 10(21): World Health Organization; 2003.

Chapter Two

Experimental Materials and Methods

The content of this chapter describes materials and established methods used throughout the thesis. No novel methodologies are presented in this chapter.

2.1 Materials

2.1.1 Tissue Collection

Human vertebral bone samples were collected from routine post-mortem examination at the Royal Adelaide Hospital, Adelaide, South Australia. All post-mortem cases were selected using the following criteria:

1. No known history of any chronic condition or disease that may have affected bone status.
2. No known history of any medication that may have affected bone turnover.
3. Admitted to hospital less than 3 days before death.
4. No macroscopic or radiological assessment of the spine or vertebral body showing signs of pathology.

Cases were excluded if there was any evidence of hepatitis or HIV from patient history or a blood test of arterial blood taken at autopsy. Spines consisting of T12 through to L5 were collected from donors, flensed and immediately wrapped in saline soaked gauze and stored at -70 ^{o}C until required.

Parasagittal Slice and Vertebral Trabecular Bone Cube

Vertebral bodies were separated from whole spines by cutting through the midline of the inter-vertebral disc separating two vertebra. Vertebral bodies were measured and marked with a permanent marker to indicate the position of the parasagittal slice and central trabecular bone cube (Figure 2.1). To locate the central region of vertebral bodies, both the mediolateral and anteroposterior mid-point of the superior face of vertebral bodies were marked by measuring the face dimensions. A 10 x 10 mm region was then marked on the superior face of the vertebral body by measuring 5 mm from the mid-point on each of the lateral left, lateral right, anterior and posterior regions. Adjustments were also made for a 1 mm border to account for saw blade thickness.

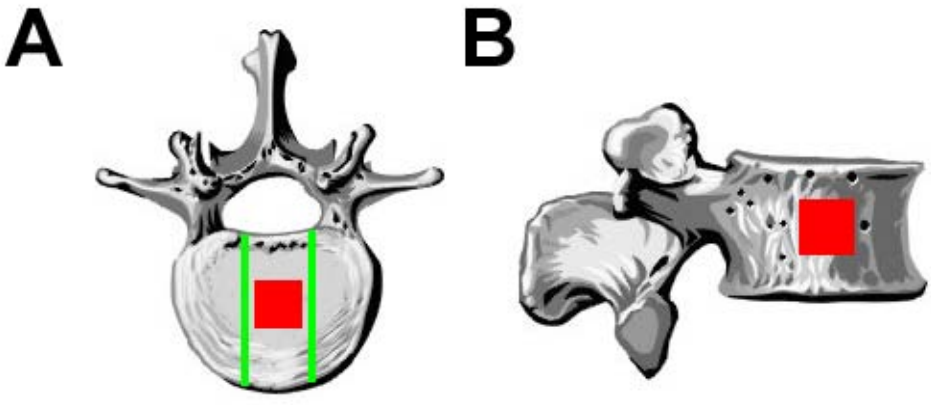

Figure 2.1 Positions of the central cube and para-sagittal slices cut from each vertebral body. (A) Axial view of a vertebral body illustrating the approximate position of the central cube [red] and parasagittal slices [green]. (B) Lateral view of a vertebral body illustrating the approximate position of the central cube [red].

Marked vertebral bodies were mounted onto a saw using a goniometer positioned perpendicular to the saw blade. This was to ensure alignment of the cutting blade relative to the vertebral body. All cutting was carried out on frozen vertebral bodies using a low speed diamond blade saw (Southbay, Model 660), under constant water irrigation. A 5 mm parasagittal slice was cut adjacent to the midline of the vertebral body avoiding the basi-vertebral foramen as outlined by Fazzalari *et al* (2006) (6). Parasagittal slices were then processed using the protocol outlined in section 2.2.6. The remaining portion of the vertebral body was re-mounted on the goniometer and the central cube was cut using the measurements marked out on the vertebral body. A goniometer was used to ensure parallel cube faces. The superior and posterior faces of the cube were marked with black and red ink, respectively.

A total of 61 vertebral bodies from T12 – L5 were processed, with the average age at death being 61.2 ± 19.3 (mean ± standard deviation) (Table 2.1). Complete sets of vertebrae, T12 – L5, could not be obtained from any one individual for this study due to other projects running within the laboratory.

Table 2.1 Details of vertebral bodies used throughout this thesis.

VERTEBRAL BODY	#	MALE	FEMALE	AGE RANGE	AV. AGE ± S.D.
T12	7	5	2	28 - 83	59.3 ± 22.2
L1	7	5	2	28 - 83	59.3 ± 22.2
L2	16	8	8	16 - 87	59.9 ± 20.8
L3	16	8	8	16 - 87	59.9 ± 20.8
L4	7	5	2	56 - 82	68.1 ± 11.1
L5	8	5	3	56 - 82	63.8 ± 16.1
TOTAL	61	36	25	16 - 87	61.2 ± 19.3

2.1.2 Ethical Considerations

Ethical approval for the collection of post-mortem vertebral material from the Royal Adelaide Hospital was granted by the Royal Adelaide Hospital/IMVS Research Ethics Committee. In all cases informed consent for use of bone tissue was obtained from next-of-kin prior to autopsy.

2.2 Methods

2.2.1 Dimension Measurements

All trabecular bone cube dimensions were measured using digital callipers (Model 500-115, Mitutoyo Corporation). For each cube, three measurements: anteroposterior depth (D_{AP}), superoinferior height (H_{SI}) and mediolateral width (W_{ML}) were made. Anteroposterior surface area was defined as the area: H_{SI} x W_{ML}, superoinferior surface area was defined as the area: D_{AP} x W_{ML} and the cube volume as: D_{AP} x W_{ML} x H_{SI}.

2.2.2 Micro-Computed Tomography

Acquisition

Trabecular bone cubes were imaged in individual polypropylene containers using a Skyscan 1072 *ex-vivo* µCT scanner (Skyscan). All cubes were imaged under the same conditions using the following settings: source voltage at 80 kVp, source current at 120 µA, magnification at 20x (equivalent to 15.631 µm per voxel), 1 mm aluminium filter, frame averaging of 4, rotation step at 0.90 degrees and rotation angle of 180 degrees.

To minimise sample movement during scanning, all cubes were left to thaw overnight prior to scanning and scanned in a hydrated environment. Once initial parameters were set, the acquisition step was completely automated and did not require operator assistance. Scan time, on average, required 1 hour and 50 minutes after which time trabecular bone cubes were re-frozen to -30 ^{o}C prior to further experimentation.

Reconstruction

From the acquisition step, 207 16-bit shadow images (Figure 2.2 [A]) (equivalent to x-ray images) were obtained. These files were the input into a cone-beam reconstruction software NRecon (Skyscan), which reconstructed the tomographic images (Figure 2.2 [B]).

Smoothing and beam-hardening correction steps were applied within NRecon to suppress noise and beam hardening artefacts, respectively. Beam hardening correction was only moderately applied (set to 10 % within NRecon) due to the use of the aluminium filter during acquisition. This filter acts to suppress low energy x-rays from the source, thus minimising beam hardening artifacts.

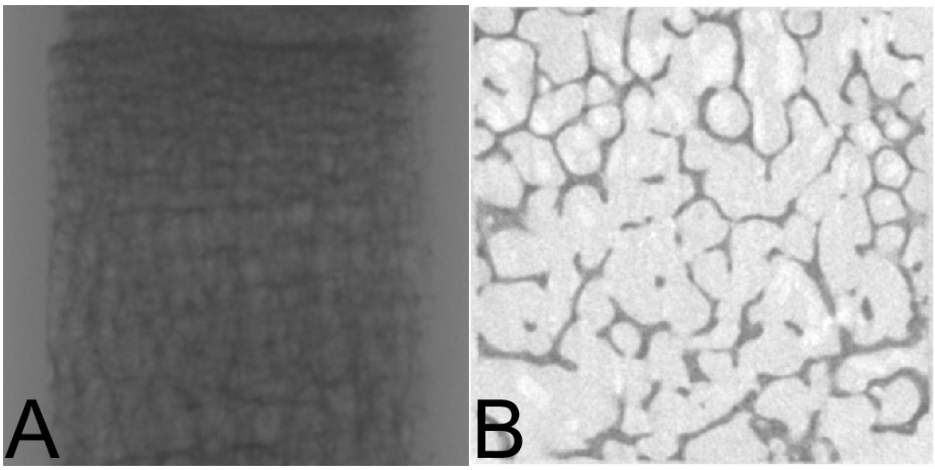

Figure 2.2 Examples of (A) shadow projection and (B) reconstructed tomographic image from µCT.

Tomographic Preprocessing

In order to suppress noise and produce smoother surfaced three dimensional (3D) models, a protocol suggested by Hildebrand *et al* (1999) (10) was employed to smooth tomographic images with a Gaussian lowpass filter prior to binarization (Figure 2.3).

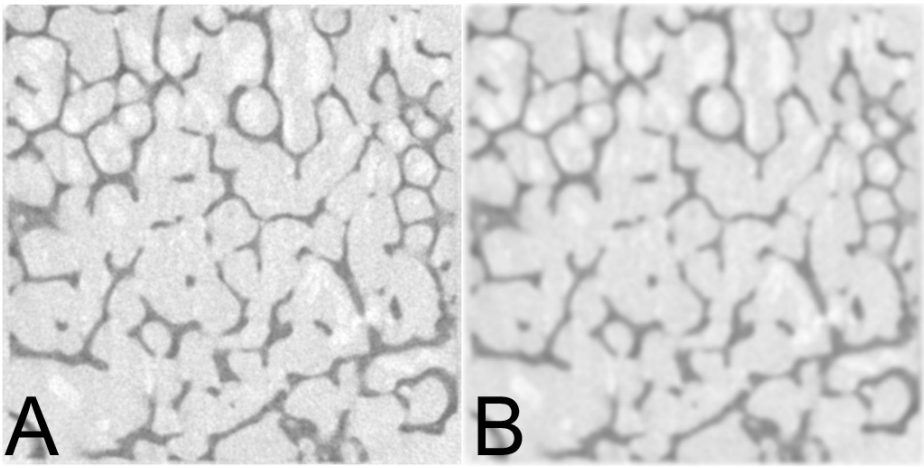

Figure 2.3 Examples of (A) original unprocessed greyscale tomograph and (B) Gaussian lowpass filtered (smoothed) tomograph.

Binarization

The majority of traditional analyses carried out on μCT images are performed on binary tomographs. Binary tomographs are segmented images of the original greyscale tomographs. In effect, the binarization process reduces the dynamic range of the original greyscale tomograph from 256 levels (for an 8-bit image) to 2 levels by discriminating which group of pixels should be assigned to non-bone and which to bone. This thresholding or segmentation process allows the bone phase and marrow (or non-bone) phase to be separated (Figure 2.4).

In this study, an automated binarization algorithm, known as Otsu's algorithm (20), was used. This was to minimize any bias and random error from operator selected thresholds. A separate study was undertaken to assess this approach, comparing three different operators with automated techniques (Appendix A).

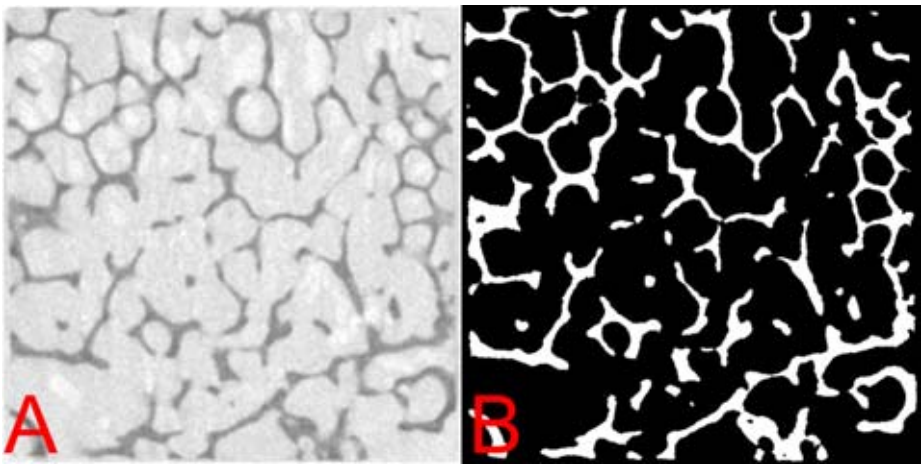

Figure 2.4 Examples of (A) grey-scale tomograph and (B) binary tomograph illustrating the separation of the bone and marrow phases.

All binarization was carried out on smoothed grey tomographic images, obtained from the reconstruction step, using a custom written application in Matlab (The Mathworks). Smoothed 8-bit grey-scale images were read from a directory, processed and binary images written as 1-bit bitmap (BMP) files.

Three Dimensional Reconstruction

Three dimensional reconstructions of samples were created by effectively stacking all 2D tomographs on top of each other; analogous to stacking slices of bread on top of each other to re-create a loaf of bread. Prior to 3D reconstruction, a component labelling algorithm, available within CTAn, was used to isolate the largest 3D connected structure and discard all other structures. All reconstructions where created in CTAn (Skyscan) using a marching cubes algorithm (15) and saved as stereo-lithography (STL) surface models. STL models were then imported into Paraview software (Kitware) for visualization (Figure 2.5).

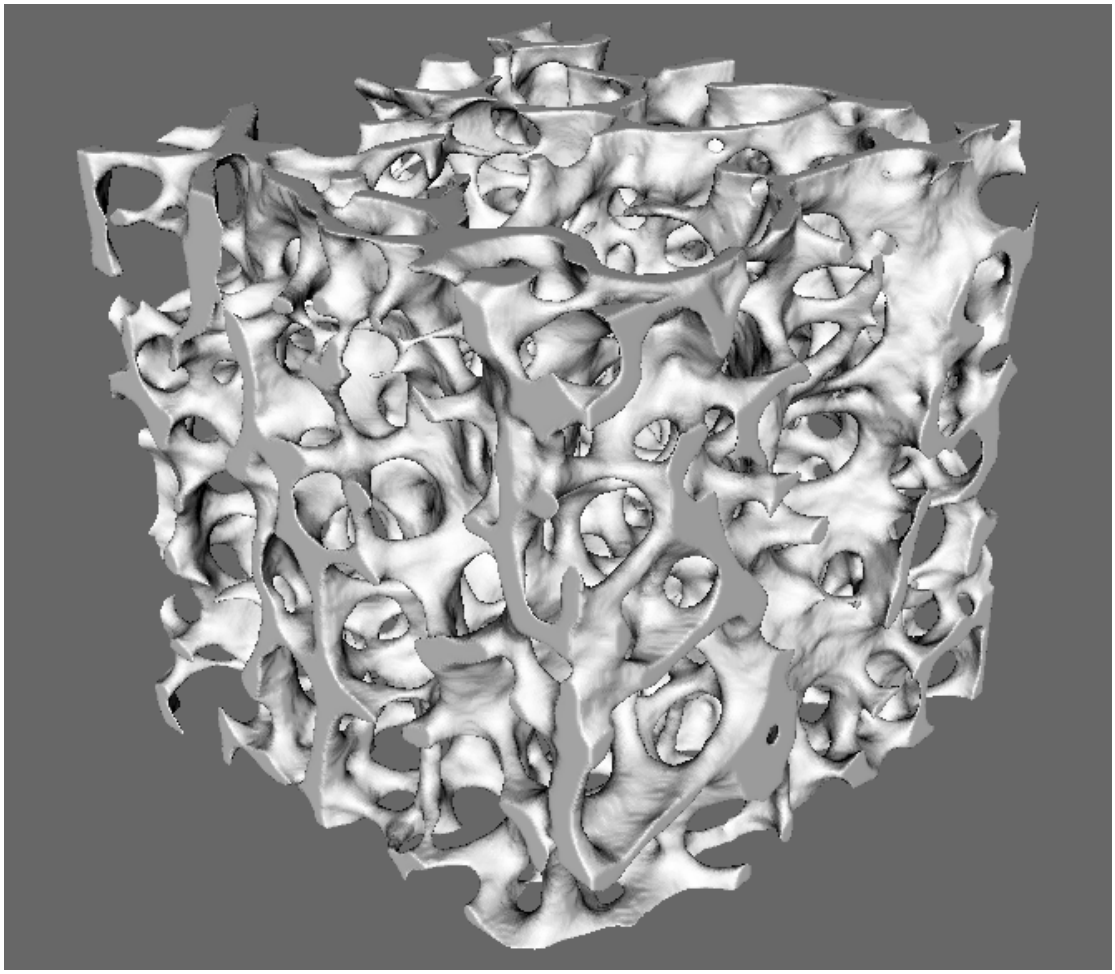

Figure 2.5 Three dimensional reconstruction of a cube of vertebral trabecular bone imaged using µCT.

Structural Analyses

A total of ten morphometric parameters were measured using CTAn software (Skyscan).

Bone Volume Fraction

Bone volume fraction (BV/TV) represents the fraction of the volume of interest (VOI) that is occupied by bone, where BV represents the bone volume and TV the tissue volume. TV is defined as the union of trabecular bone volume and marrow space volume ($TV = |Bone \cup Marrow|$).

$$\therefore \frac{BV}{TV} = \frac{|Bone|}{|Bone \cup Marrow|} \text{ and } Marrow\ Volume\ Fraction = \frac{|Marrow|}{|Bone \cup Marrow|},$$

$$\therefore \frac{BV}{TV} + Marrow\ Volume\ Fraction = 1.$$

Specific Surface

Specific surface (BS/BV) represents the bone surface (BS) relative to the bone volume (BV). BS is calculated as the total area of triangles resulting from the triangulation of the surface of voxels in the 3D model using the marching cubes algorithm (15).

Total Surface

Total surface (BS/TV) represents the bone surface (BS) relative to the tissue volume (TV) of the VOI. Bone surface (BS) was calculated in the same manner as for specific surface (BS/BV).

Trabecular Thickness

Trabecular thickness (Tb.Th) represents the mean thickness of trabecular elements in the VOI and can be measured using either model-dependent or model-independent measures of thickness.

Model-dependent measures of geometric parameters are based on assumptions of fixed structural models. These methods allow derivation of 3D structural parameters from 2D histological measurements of bone area fraction and bone perimeter through well established stereological principles (21, 24). The parallel-plate model (11, 21) models the trabecular structure as a series of parallel plates (Figure 2.6). Given the measurement of BV/TV and BS/TV described above,

$$\mathrm{Tb.Th} = 2.\frac{\mathrm{BV}}{\mathrm{BS}}. \qquad 2.1$$

3D model-independent measurements of Tb.Th ($\mathrm{Tb.Th_{3D}}$) were calculated via direct 3D morphometric analyses as described by Hildebrand and Ruegsegger (1997) (11). Here Tb.Th is calculated as the average of the local maximal thicknesses along the distance transform of the 3D structure (10, 11).

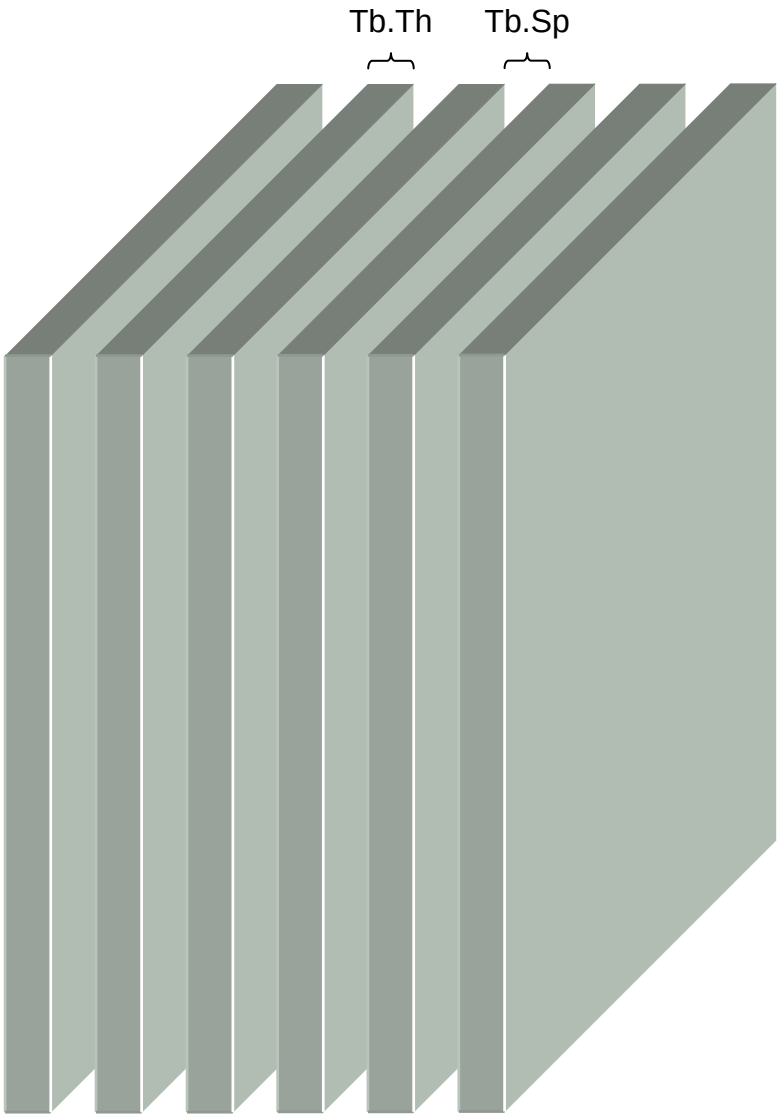

Figure 2.6 Illustration of the parallel-plate model.

Trabecular Number

Trabecular number (Tb.N) is a linear density measure representing the number of intersections made across a trabecular structure for a linear path through the trabecular structure (21, 24). Similar to Tb.Th, both model-dependent and model-independent techniques can be employed. For the parallel-plate model (21),

$$\mathrm{Tb.N} = \frac{(\mathrm{BS}/\mathrm{TV})}{2}. \qquad 2.2$$

3D model-independent measurement employs use of 3D model-independent $\mathrm{Tb.Th_{3D}}$ and BV/TV measured from the 3D structure. Thus, for the 3D model-independent technique,

$$\mathrm{Tb.N_{3D}} = \frac{(\mathrm{BV}/\mathrm{TV})}{\mathrm{Tb.Th_{3D}}}. \qquad 2.3$$

Trabecular Separation

Trabecular separation (Tb.Sp) is a measure of the separation between the edges of trabecular elements (21). Similar to Tb.Th and Tb.N, Tb.Sp can be measured using both model-dependent and model-independent techniques. Using the parallel-plate model (21),

$$\mathrm{Tb.Sp} = \left(\frac{1}{\mathrm{Tb.N}}\right) - \mathrm{Tb.Th}. \qquad 2.4$$

3D model-independent measurement of Tb.Sp ($\mathrm{Tb.Sp_{3D}}$) is made using the same technique as that for calculating $\mathrm{Tb.Th_{3D}}$, except that the algorithm is applied to non-bone voxels of the 3D structure (10, 11).

Degree of Anisotropy

Degree of anisotropy (DA) is a measure of preferential alignment. For a detailed description of DA, refer to Chapter 3. Briefly, in CTAn, DA is calculated using information obtained from assessment of the mean intercept length (MIL). The MIL is found by dividing the length of test lines in 3D by the number of intersections between these test lines and the trabecular structure. The DA is then derived from the eigenvalues resulting from the best-fitting ellipsoid to the 3D MIL data, where DA is the ratio of maximum eigenvalue to minimum eigenvalue (18, 19).

Trabecular Bone Pattern Factor

Trabecular bone pattern factor (TBPf) quantitatively describes the ratio of inter-trabecular connectivity by calculating an index of relative surface convexity or concavity (8). TBPf calculates the bone volume (BV) and bone surface (BS) before and after a simulated dilation and is defined as the quotient of the difference,

$$\mathrm{TBPf} = \frac{\mathrm{BS}_{\mathrm{BEFORE}} - \mathrm{BS}_{\mathrm{AFTER}}}{\mathrm{BV}_{\mathrm{BEFORE}} - \mathrm{BV}_{\mathrm{AFTER}}}. \qquad 2.5$$

In the case of well connected trabecular bone, TBPf leads to low values and in the case of isolated trabeculae results in higher values (8).

Structure Model Index

The structure model index (SMI) was developed by Hilderbrand and Ruegsegger (1997) as a way of quantifying the prevalence of plate-like and rod-like elements within a trabecular structure (12). Similar to the TBPf, SMI is based on calculation of bone volume and bone surface (BS). However, unlike the TBPf, SMI only calculates the BS before and after simulated dilation and is defined as,

$$SMI = 6 \times \left(\frac{BS_{AFTER} \times BV}{BS_{BEFORE}^{2}} \right). \qquad 2.6$$

In the case of an ideal plate, ideal cylinder and ideal sphere, the SMI has values 0, 3 and 4, respectively (12).

Connectivity Density

Connectivity is a measure of the number of redundant elements in the trabecular bone structure (18). Connectivity centres around the Euler number (18, 19) (χ), where in a 3D trabecular structure with β_1 redundant connections,

$$\chi = 1 - \beta_1. \qquad 2.7$$

CTAn (Skyscan) determines the Euler number using the ConnEulor principle described by Gundersen *et al* (1993), where the Euler number is calculated by measuring topological changes between pairs of consecutive sections (tomographs) within a 3D structure (7, 18). The connectivity density (Conn.D) is then defined as,

$$Conn.D = \frac{\beta_1}{TV}. \qquad 2.8$$

2.2.3 Dual Energy X-ray Absorptiometry

All scans were taken on a GE-Lunar Prodigy Vision (GE Healthcare) scanner in the bone densitometry section of the Department of Nuclear Medicine, PET and Bone Densitometry at the Royal Adelaide Hospital, Adelaide, South Australia.

Whole Spine Assessment

A protocol was used to image whole spines collected from post-mortem examination to closely mimic clinical *in-vivo* assessment. This protocol consisted of placing whole spines (T12 – L5) in a container along with water bags. The water bags were used to simulate soft tissue to a depth of 15 cm. Care was taken to minimise air pockets between the spine and the water bags. Correct anteroposterior alignment of the spine with respect to the scanner was first verified by gross visual inspection and then on the scanned image. Bone mineral density (BMD) of the individual vertebral bodies (BMD_{IND}) and the average BMD of L2 – L4 vertebral bodies (BMD_W) were obtained. Based on the BMD_W the T score and Z score were also calculated. The T score is a linear transform of the BMD and represents the number of standard deviations above or below a young normal reference. The Z score is similar to the T score except that it represents the number of standard deviations above or below an age, sex and race matched reference. Both the T and Z scores provide a means of comparing the BMD of an individual with that of a "normal" population (13, 27).

Trabecular Bone Cube Assessment

Bone mineral content (BMC) of trabecular bone cubes was measured using specialised small specimen software algorithms available on the DXA scanner (Prodigy Vision version 9.15, GE-Lunar). Multiple cubes were analysed in a single scan and results reported as individual BMC (g). Areal and volumetric BMD were then calculated by normalising the BMC by the cube's anteroposterior area and volume respectively (Section 2.2.1).

2.2.4 Biomechanical Testing

All mechanical testing was carried out on a universal testing machine (Hounsfield, H25KM) controlled by a personal computer and custom designed software. The compressive load was produced by displacement (at a rate of 1 mm/min) of a screw-driven upper platen onto unsupported samples placed on a lower fixed platen (5, 16, 17, 26). A layer of latex of thickness 0.14 mm was used on each end of the bone cubes to provide stability for free trabecular ends and maximize the contact area between sample and the machine (5). To minimize the effects of misalignment, a pivoting platen was used in the load train (17, 26). Extension was measured by displacement of platens. No pre-conditioning (14) was carried out on samples prior to testing. All load-extension information was recorded and saved on the controlling PC. Extension (mm) was converted to strain (mm / mm) by subtracting the extension at 5 N pre-load from the instantaneous extension and normalizing by the dimension of the cube parallel to the load-train (original height),

$$\text{Strain}(\text{mm}/\text{mm}) = \frac{\text{Extension}(\text{mm}) - \text{Extension}_{5\text{N}}(\text{mm})}{\text{Original Height}\,(\text{mm})}. \qquad 2.9$$

Load was converted to stress by normalizing the instantaneous load by the surface area to which the load was being applied,

$$\text{Stress}\,(\text{MPa}) = \frac{\text{Load}\,(\text{N})}{\text{Area}\,(\text{m}^2)}. \qquad 2.10$$

The ultimate failure stress (UFS), ultimate failure strain (UFSt), yield stress (YS), yield strain (YSt) and modulus of elasticity (E) were calculated from the resulting stress-strain curve (Figure 2.7). UFS was defined as the stress at the maximal point of the stress-strain curve, UFSt as the strain at the point of UFS, YS as the stress separating the elastic and plastic regions of the stress-strain curve, YSt as the strain at the point of yield and E as the maximum slope of the elastic portion of the stress-strain curve (1, 16, 26).

Since the point of yield is typically not self evident and subtle on stress-strain curves resulting from the compression of trabecular bone samples, a procedure known as the 0.2 % offset method was used. Here the point of yield was defined as the intersection of a line parallel to but offset by 0.2 % from the elastic (linear) portion of the stress-strain curve (22, 26) (Figure 2.7).

Other mechanical variables such as the modulus of toughness (u_T) and modulus of resilience (u_R) were also measured. The modulus of toughness, the area under the stress-strain curve up to the point of failure (Figure 2.8), represents the amount of energy required to cause failure of the sample (1, 22). Modulus of resilience, the area under the stress-strain curve up to the point of yield (Figure 2.9), represents the amount of energy that the sample is able to absorb without causing permanent damage (1, 22).

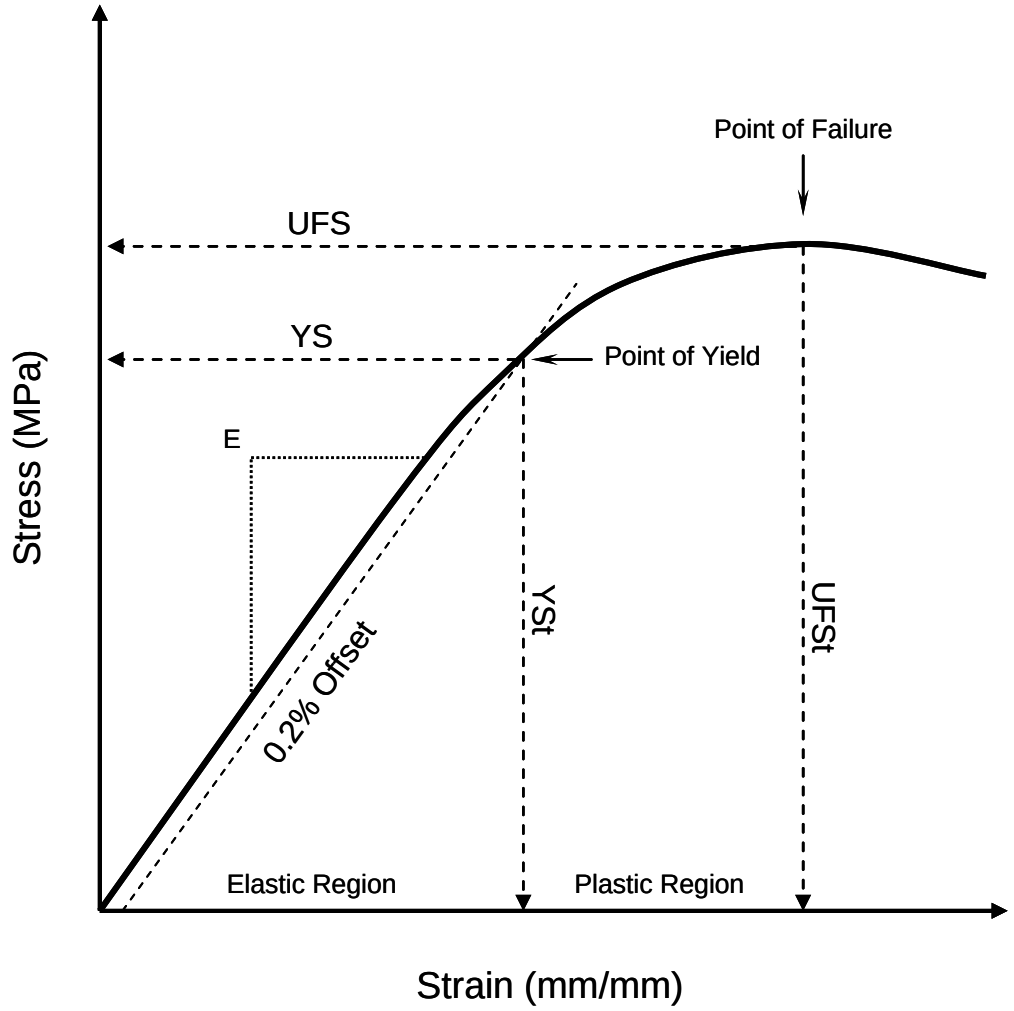

Figure 2.7 Typical stress-strain curve for the compression of trabecular bone. The stress-strain curve is divided into elastic and plastic regions, separated by the point of yield. This point of yield is found using a technique known as the 0.2% offset method. The ultimate failure stress (UFS) is the maximal stress, the ultimate failure strain (UFSt) represents the strain at maximal stress, yield stress (YS) is the stress at the point of yield, yield strain (YSt) represents the strain at the point of yield and elastic modulus (E) is the maximum slope of elastic region of the stress-strain curve.

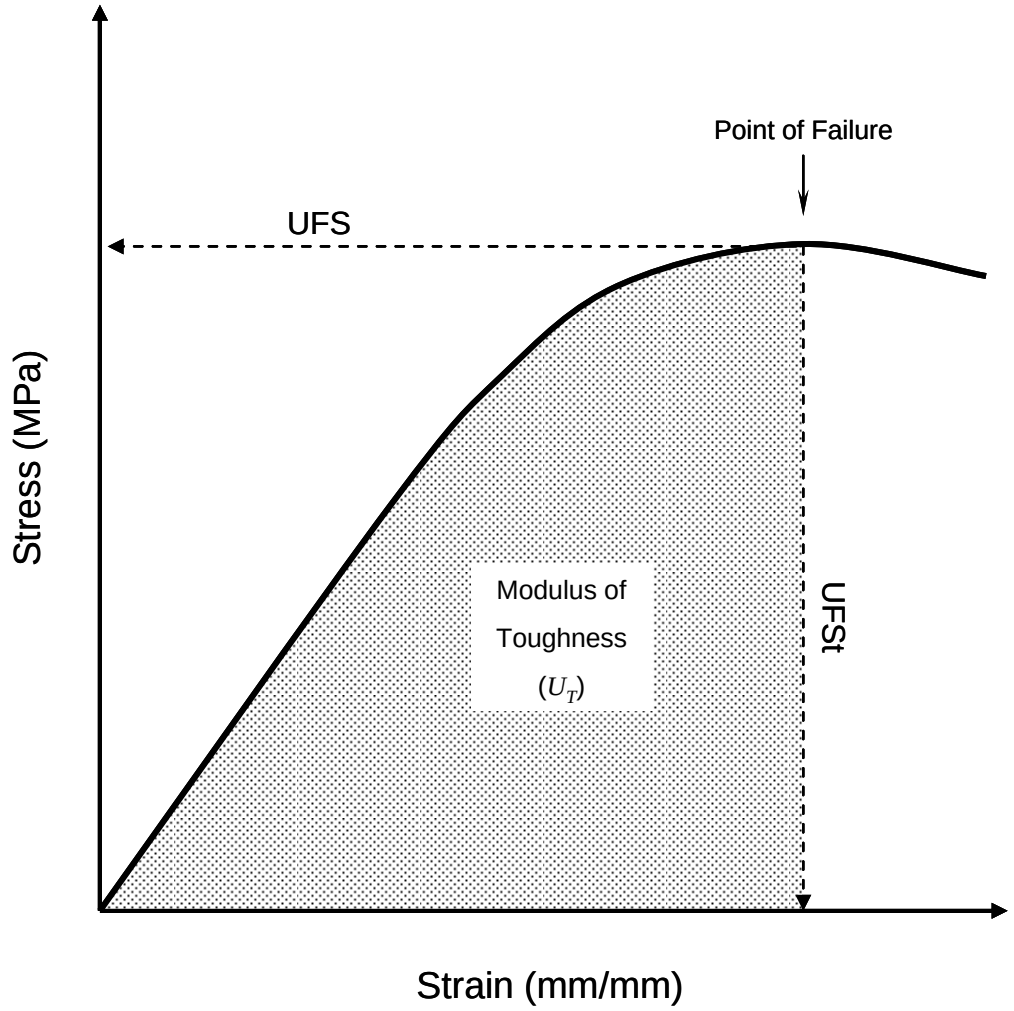

Figure 2.8 Typical stress-strain curve for the compression of trabecular bone. The modulus of toughness of the sample is defined as the area under the stress-strain curve up to the point of failure. Modulus of toughness represents the amount of energy required to cause catastrophic failure of the sample.

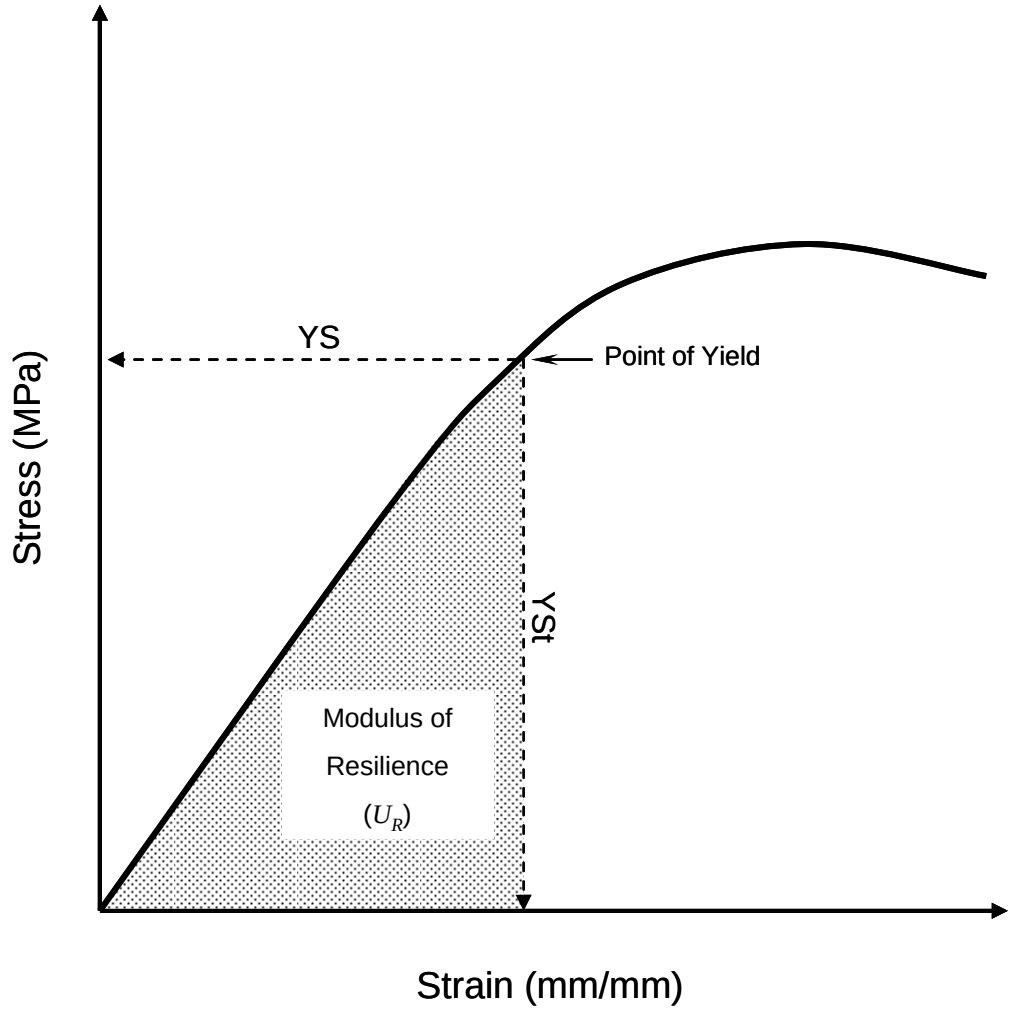

Figure 2.9 Typical stress-strain curve for the compression of trabecular bone. The modulus of resilience of the sample is defined as the area under the stress-strain curve up to the point of yield. Modulus of resilience represents the amount of energy that the sample is able to absorb without causing permanent damage.

2.2.5 Ashing

Ashing was carried out as the final step in experiments involving bone tissue to determine true mineral content of samples. Samples were initially weighed to determine their wet weight (W_{WET}). All samples were placed in small ceramic crucibles with known (measured) weight (W_{CRUC}). All ashing was carried out in a temperature and time controlled furnace (Jetflow). Ashing consisted of three consecutive steps: 160 ^{o}C for 12 hours, 400 ^{o}C for 12 hours and 800 ^{o}C for 12 hours, following the protocols outlined in the literature (3, 4). After each step, the weight of the crucible (containing the sample) was recorded (W_{160}, W_{400} and W_{800}, respectively). Sample weight was determined by subtracting the initial crucible weight (W_{CRUC}) from the combined crucible-sample weight after each step. The final weight measurement ($W_{800} - W_{CRUC}$) was recorded as the bone mineral content (BMC). Areal and volumetric density calculations were made by normalising the BMC by the anteroposterior area and volume of the sample (section 2.2.1), respectively.

2.2.6 Semi-Interactive Analysis of Cortical Thickness

Though parasagittal slices were used for measurements of vertebral cortical thickness, this information was not used in this thesis. However, for completeness a description of measurement methodologies is presented here.

A semi-interactive method was used to measure the cortical thickness of vertebral bodies from 5 mm parasagittal slices collected from vertebral samples following the protocol suggested by Fazzalari *et al* (2006) (6). Briefly, slices were cut close to the midline of the vertebral body (Figure 2.1) and fixed using 10% neutral buffered formalin and decalcified with 9% nitric acid in 1% EDTA. After appropriate embedding in paraffin wax, 7 µm sections were cut from each block using a sledge microtome (Leica) and mounted on slides. Slides were stained with van Gieson stain to provide clear distinction between bone matrix and other tissues.

Each vertebral body section was divided into nine equal sectors (Figure 2.10), dividing the anterior and posterior cortical walls into three regions with adjacent trabecular bone sectors, as outlined by Simpson *et al* (2001) (25). Verification that the stained material was cortical bone was made by examining slides under polarized light. Anterior and posterior cortical thicknesses were measured by tracing the cortical shell with a computer mouse pointer to produce a binary representation of the cortical shell. This binary representation was converted into a series of chords by performing a binary AND operation between the binary representation of the cortical shell and a binary image consisting of multiple parallel lines, 1 pixel apart and perpendicular to the cortical shell. The resulting binary chords are representative of the thickness of the cortical shell. The mean cortical thickness (Ct.Th) for each region was calculated as the mean length of the binary chords. All analyses were carried out on a Quantimet Image Analyser (Leica DM6000B & Q550IW).

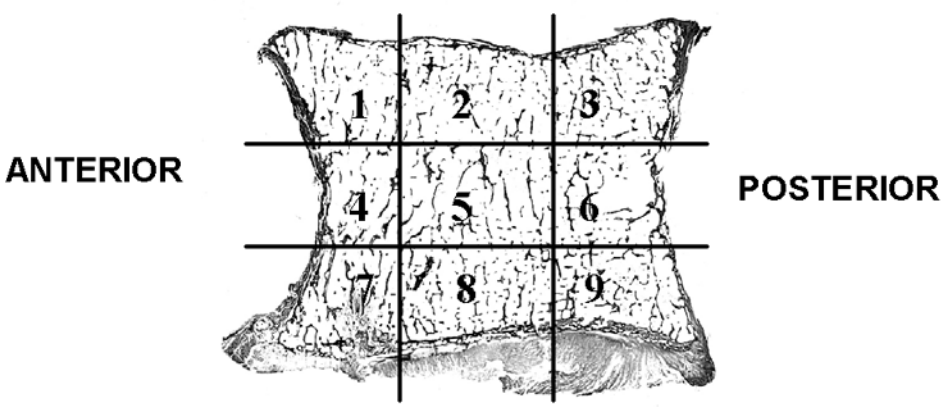

Figure 2.10 Example of a sagittal vertebral slice and the subsequent regions marked and used for measurement of cortical thickness.

2.2.7 Radon Transform

The Radon transform is defined as the projection of an image I(i,j) along projection lines, at all angles θ, where the image is mapped from the image plane (i,j) to the projection plane (θ, x) (2, 23).

If a series of parallel projections are measured, an intensity profile is obtained (Figure 2.11). The resulting function, S(θ, x), is the summation of absorption along each path. This function varies with both the position along the direction, x, as the projection path samples different portions of the object and also with orientation, θ (23). For each orientation, θ, a one-dimensional (1D) projection as a function of position, x, is obtained. The collection of these, for many orientations can be presented in a 2D image where x forms one axis and θ the other (23). This image is the visualisation of the Radon transform (Figure 2.12 [B] and [C]).

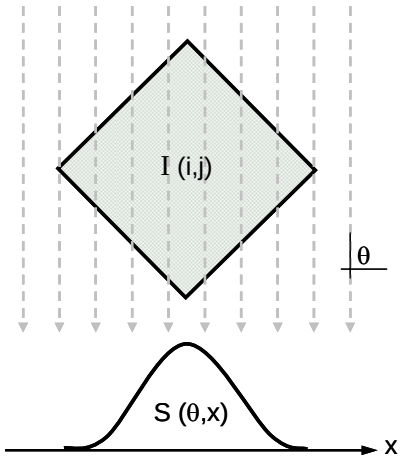

Figure 2.11 Illustration of a projection through an object at a viewing angle θ forming the function S(θ, x), the Radon transform.

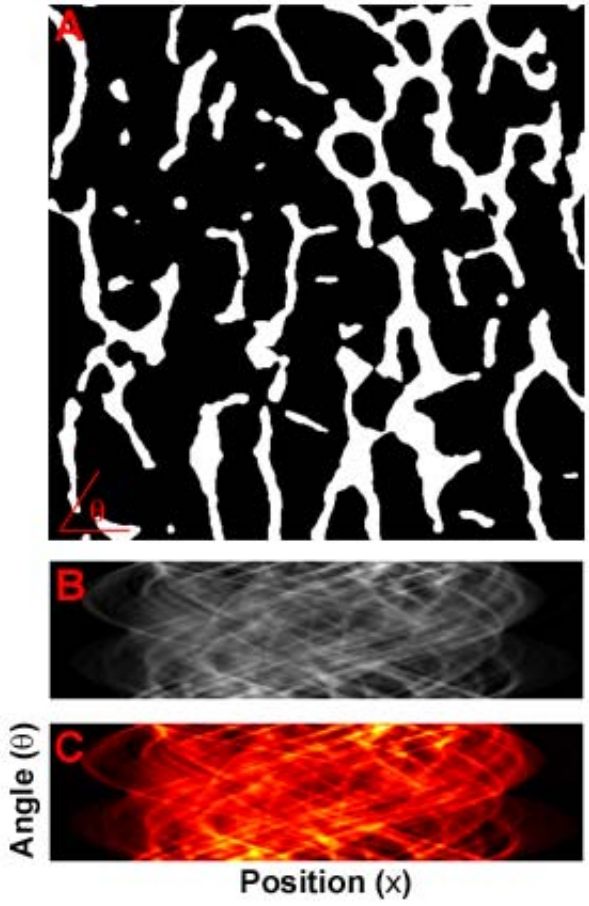

Figure 2.12 Radon transform. [A] Tomographic image of human trabecular bone (refer to Chapter 3), [B] Radon transform of [A] computed at 1^o intervals for $0^o \leq \theta < 180^o$ and [C] Radon transform shown in false colour.

Mathematically, the Radon transform is defined as,

$$S(\theta, x) = \int_{-\infty}^{\infty}\int_{-\infty}^{\infty} I(i, j)\delta(i\cos\theta + j\sin\theta - x)didj\,, \qquad 2.11$$

If $S(\theta, x)$ is known for all $\theta \in [0, \frac{\pi}{2})$ and $x \in (-\infty,\infty)$, then the Radon transform is invertible and so the image I can be fully recovered from $S(\theta, x)$ without loss (2, 23).

In practice, data from only finitely many directions θ are available and these are used to obtain approximate reconstructions (9).

Inverse Radon Transform

The inverse Radon transform is concerned with the reconstruction of an image I(i,j) given the Radon transform, $S(\theta, x)$, of the image. There are several ways in which to compute the inverse Radon transform. It is beyond the scope of this thesis to discuss these techniques. It is sufficient for the reader to recognise that the inverse Radon transform reconstructs a tomographic image from the Radon transform of the image (Figure 2.13).

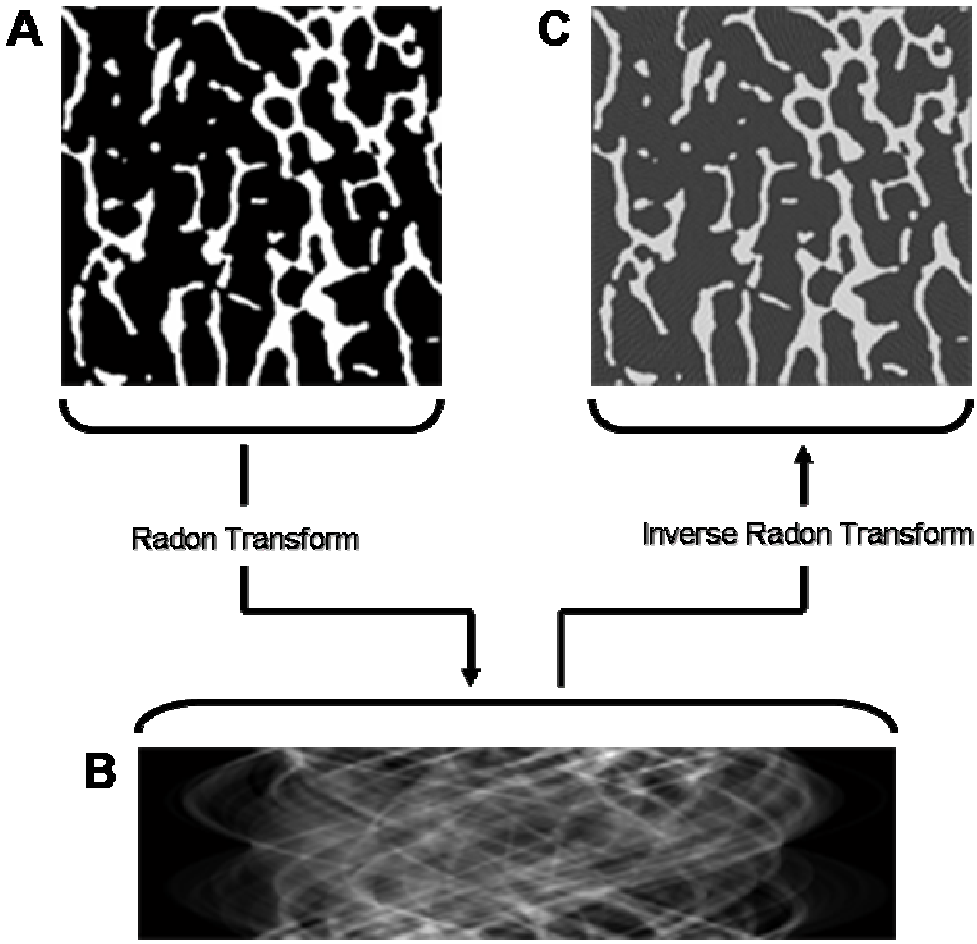

Figure 2.13 Processes of Radon and Inverse Radon transforms, [A] Binary tomographic image, [B] Radon transform of [A] computed at 1^o intervals for $0^o \leq \theta < 180^o$ and [C] Reconstructed image computed from Radon transform in [B] using inverse Radon transform.

References

1. Askeland, D. R. The Science and Engineering of Materials: Stanley Thornes (Publishers) Ltd; 1996.
2. Bocchi, L., and Nori, J. Shape analysis of microcalcifications using Radon transform. Med Eng Phys 29:691-8; 2007.
3. Boskey, A. L. Bone Mineralization. In: S. C. Cowin (ed.), Bone Mechanics Handbook, pp. 5/1 - 5/33: CRC Press; 2001.
4. Ebbesen, E. N., Thomsen, J. S., Beck-Nielsen, H., Nepper-Rasmussen, H. J., and Mosekilde, L. Lumbar vertebral body compressive strength evaluated by dual-energy X-ray absorptiometry, quantitative computed tomography, and ashing. Bone 25:713-24; 1999.
5. Fazzalari, N. L., Forwood, M. R., Smith, K., Manthey, B. A., and Herreen, P. Assessment of cancellous bone quality in severe osteoarthrosis: bone mineral density, mechanics, and microdamage. Bone 22:381-8; 1998.
6. Fazzalari, N. L., Parkinson, I. H., Fogg, Q. A., and Sutton-Smith, P. Antero-postero differences in cortical thickness and cortical porosity of T12 to L5 vertebral bodies. Joint Bone Spine 73:293-7; 2006.
7. Gundersen, H. J., Boyce, R. W., Nyengaard, J. R., and Odgaard, A. The Conneulor: unbiased estimation of connectivity using physical disectors under projection. Bone 14:217-22; 1993.
8. Hahn, M., Vogel, M., Pompesius-Kempa, M., and Delling, G. Trabecular bone pattern factor--a new parameter for simple quantification of bone microarchitecture. Bone 13:327-30; 1992.
9. Herman, G. T. Image Reconstruction From Projections. New York: Academic Press; 1980.
10. Hildebrand, T., Laib, A., Muller, R., Dequeker, J., and Ruegsegger, P. Direct three-dimensional morphometric analysis of human cancellous bone: microstructural data from spine, femur, iliac crest, and calcaneus. J Bone Miner Res 14:1167-74; 1999.
11. Hildebrand, T., and Ruegsegger, P. A new method for the model-independent assessment of thickness in 3D images. Journal of Microscopy 185:67-75; 1997.
12. Hildebrand, T., and Ruegsegger, P. Quantification of Bone Microarchitecture with the Structure Model Index. Comput Methods Biomech Biomed Engin 1:15-23; 1997.
13. Kanis, J. A., Delmas, P., Burckhardt, P., Cooper, C., and Torgerson, D. Guidelines for diagnosis and management of osteoporosis. The European Foundation for Osteoporosis and Bone Disease. Osteoporos Int 7:390-406; 1997.
14. Keaveny, T. M., Pinilla, T. P., Crawford, R. P., Kopperdahl, D. L., and Lou, A. Systematic and random errors in compression testing of trabecular bone. J Orthop Res 15:101-10; 1997.
15. Lorensen, W. E. C., H.E. Marching cubes: A high resolution 3D surface construction algorithm. Proceedings of the 14th annual conference on Computer graphics and interactive techniques:163 - 169; 1987.
16. Mosekilde, L., and Danielsen, C. C. Biomechanical competence of vertebral trabecular bone in relation to ash density and age in normal individuals. Bone 8:79-85; 1987.
17. Mosekilde, L., and Viidik, A. Correlation between the compressive strength of iliac and vertebral trabecular bone in normal individuals. Bone 6:291-5; 1985.
18. Odgaard, A. Quantification of Cancellous Bone Architecture. In: S. C. Cowin (ed.), Bone Biomechanics Handbook, 14/1 - 14/19, Second Edition, CRC Press, 2001.
19. Odgaard, A. Three-dimensional methods for quantification of cancellous bone architecture. Bone 20:315-28; 1997.
20. Otsu, N. A Threshold Selection Method from Gray-Level Histograms. IEEE Transactions on Systems, Man, and Cybernetics 9:62 - 66; 1979.
21. Parfitt, A. M., Drezner, M. K., Glorieux, F. H., Kanis, J. A., Malluche, H., Meunier, P. J., Ott, S. M., and Recker, R. R. Bone histomorphometry: standardization of nomenclature, symbols, and units. Report of the ASBMR Histomorphometry Nomenclature Committee. J Bone Miner Res 2:595-610; 1987.
22. Roylance, D. Stress-Strain Curves. Cambridge, MA; 2001.
23. Russ, J. C. Image Processing Handbook: CRC Press; 2002.
24. Russ, J. C., and Dehoff, R. T. Practical Stereology. New York: Plenum Publishers; 2000.
25. Simpson, E. K., Parkinson, I. H., Manthey, B., and Fazzalari, N. L. Intervertebral disc disorganization is related to trabecular bone architecture in the lumbar spine. J Bone Miner Res 16:681-7; 2001.
26. Turner, C. H. and Burr, D. B. Experimental Techniques for Bone Mechanics. In: S. C. Cowin (ed.), Bone Mechanics Handbook, pp. 7/1 - 7/35, Second Edition, CRC Press, 2001.
27. WHO Technical Report Series (Prevention and Management of Osteoporosis) - Diagnosis and Assessment. In: W. S. G. o. P. a. M. o. Osteoporosis (ed.), WHO Scientific Group on Prevention and Management of Osteoporosis, pp. 53(33): World Health Organization; 2003.